SPECTRAL QUALITY EVALUATION OF RECONSTRUCTED HYPERSPECTRAL IMAGES

Shimin Tang[1], Zhiqiang Chen[2]and Molan Zhang[3]
[1,3]Doctoral students, Department of Computer Science and Electrical Engineering, University of Missouri-Kansas City
[2]Associate Professor, Department of Civil and Mechanical Engineering, University of Missouri-Kansas City

ABSTRACT

With the advance in imaging optics, hyperspectral images (or cubes) have become low-cost and real-time for acquiring images in the field, specifically thanks to the recent development of different 'snapshot' hyperspectral imaging systems. However, cameras producing high resolutions in both the spectral domains and the spatial domains are still rare or considered to be high-cost. Algorithm-based pansharpening, or in general image reconstruction methods, are often used to create high spatial-resolution cubes by fusing high-spatial gray or color images and low spatial-resolution hyperspectral images. Moreover, most of these methods emphasized achieving high visual quality in spatial resolution but not considering the spectral accuracy in the reconstructed images. This paper aims to evaluate the spectral quality of reconstructed images from multiple methods. A commercial hyperspectral camera (Cubert S185) was used to conduct the research. Important conclusions include that spectral information is lost to different degrees per different reconstruction methods when the spatial resolution is raised too high. The trade-off between spatial sharpening and retaining spectral information is important for machine learning tasks.

Index Terms— Hyperspectral image, Super Resolution, Spectrum analysis

1. INTRODUCTION

Hyperspectral images (HSIs), which contain both spatial and spectral information in pixels, have become a powerful media for multiple research fields[1-3]. Even in the visible and near-infrared (VNIS) range, the spectral values can provide information that is invisible to human eyes and lead to more discriminative and stable characterization for different objects in terms of spectral profiles (not a finite set of values, e.g., RGB values). For example, in agriculture, hyperspectral images can be used to discern ripe and non-ripe fruits, stressed leaves, or the material composition of dirt. Moreover, the HSIs are recently utilized more commonly in both academic research and commercial fields because of the development in hyperspectral imagery manufacture.

Snapshot cameras can capture HSIs in one shoot without sensor motion or amounting optical filters [4]. This mechanism is able to obtain HSIs without moving sensors required in push-broom cameras, hence avoiding vibration noise and reducing imaging time[5]. This new imaging mechanism dramatically enhances operability and efficiency, such that a large number of hyperspectral images can be produced in fields. In recent years, many snapshot HS cameras are commercially available[6]. In this paper, we have adopted one commercial system, the Cubert S185 system, and the hyperspectral images from this camera are concerned. The Cubert system composes of one VNIS snapshot camera and one mini-computer for real-time computing. The camera captures within the spectral bands from 440 nm to 996 nm with a 4-nm sampling width (leading to 139 spectral bands). During the imaging, the optical sensor will simultaneously take one high-spatial-resolution (1000×1000) panchromatic (gray) image and one low spatial-resolution spectral cube (50×50×139). Then the computer applies a pan-sharpening step to create a high-spatial-resolution cube with a user-defined pan-sharpening ratio. By taking the maximum ratio (i.e., 20), one can obtain a 1000×1000×139 cube. This sharpening method realizes a reconstruction procedure by fusing a low-spatial-resolution cube and its accompanied high-spatial-resolution gray image. In the literature, many reconstruction methods have been developed, which can be adopted to realize such sharpening for our imaging system at hand. However, most existing efforts aim to realize the visual resemblance of the spectral cube to the gray (or color) image [7, 8]. On the other hand, less research attempts to study the quality of spectral reconstruction. Additionally, the current methods often start with an existing HSI cube, downsample it into a cube of lower spatial resolution, then treat it ground-truth. The reconstructed cube is then compared against this ground truth to produce performance metrics. This process does not reflect the real-world situation wherein the desired high-spatial-resolution HSI cube does not exist as a ground truth.

This paper aims to evaluate the spectral quality of reconstructed HSI images, in which we will evaluate the native pansharpening method from the Cubert camera system ('Cubert Method') and a number of other reconstruction methods. In addition, in our evaluation, ground-truth HSI cubes do not exist, which is termed *non-reference evaluation*. More importantly, the authors focus on the quality evaluation in the reconstructed spectral domain.

2. EVALUATION METHODOLOGY

In order to evaluate the spectral quality of the reconstructed HSI, the 50×50 HSI taken by the Cubert camera is reconstructed by a variety of methods and compared with the Cubert method. The methods used for reconstruction include 1). Ratio Component Substitution (RCS) sharpening[9]; 2). Local Mean and Variance Matching (LMVM) sharpening[10]; 3). Bayesian Fusion sharpening[11]; and 4). Exploiting clustering manifold structure super-resolution[12]. This paper focused on evaluating the spectral quality of the above reconstructed HSIs, and the spatial quality will also be evaluated as an auxiliary reference. The spectrum quality is assessed from the aspects of spectrum consistency and spectrum composition. And three non-reference image quality metrics in the spatial domain are also calculated. Besides, this research also discussed the impact of high-resolution reconstruction on subsequent processes, such as classification or object detection. Thus, a primary Support Vector Machine (SVM)[13] is trained with 80% of pixels in one HSI, and the rest of the pixels are used for testing SVM.

2.1. High-Spatial-Resolution HSI Reconstructions

To reconstruct the low-spatial-resolution cube (50×50×139) to high-spatial-resolution (1000×1000×139) HSI, we use five different methods (include Cubert method) as mentioned. The first three sharpening methods (RCS, LMVM, and Bayesian Fusion) are implemented by using Orfeo ToolBox[14]. RCS method is a straightforward operation that fuses orthorectified panchromatic (*PAN*) and multispectral (*XS*) images using a low pass sharpening filter, and the computation equation is denoted as below:

$$Y = \frac{XS}{Low\ Pass\ Filter(PAN)} \times PAN$$

where Y is the fused image. With the same component-substitution idea, LMVM uses the filter to apply a normalization function at a local scale within the low-resolution cube to equate the local mean and variance values in the high-spatial-resolution panchromatic image. The highlight computation is expressed as:

$$Y_{i,j} = \frac{(H_{i,j} - \overline{H_{i,j}}) \times s \times (L)_{i,j(w,h)}}{s \times (H)_{i,j(w,h)}} \times E$$

where $Y_{i,j}$ refers to the fused image, $H_{i,j}$ and $L_{i,j}$ denotes high-spatial-resolution panchromatic image and low-spatial-resolution HSI respectively at pixel coordinates i,j. $(H)_{i,j(w,h)}$ and $(L)_{i,j(w,h)}$ are local means calculated inside the window of size (w, h). s denotes the local standard deviation.

The third sharpening method is Bayesian data fusion[11], which is based on statistical relationships between the various spectral bands and the panchromatic band. The indirectly observed vector is denoted as $\boldsymbol{Z}$. An error-like model links $\boldsymbol{Z}$ to spectrums $\boldsymbol{Y}$ in a high-spatial-resolution image. The model is denoted as:

$$Y = g(Z) + E$$

where $g(\boldsymbol{Z})$ is a set of functionals, and $\boldsymbol{E}$ is a random error vector is stochastically independent of $\boldsymbol{Z}$. Besides, the conditional probability density function of vector $\boldsymbol{Z}$ is:

$$f(z|y) \propto f_z(z) f_E(y - g(z))$$

where $f_Z(.)$ is the a priori pdf for $\boldsymbol{Z}$ and $f_E(.)$ is the a priori pdf of the errors E.

The last reconstruction method is manifold-based super-resolution[12]. This method firstly conducts clustering in the spatial domain of the input high-spatial-resolution image. And then, the intra-cluster self-expressiveness is adopted on clusters to create the clustering manifold structure. Then, the learned manifold structure is introduced into a variational super-resolution framework to produce the high-spatial-resolution HSI. This fusion-based super-resolution method reconstructs high-spatial-resolution HSI ($\boldsymbol{Z}$) from low-spatial-resolution HSI ($\boldsymbol{X}$) and a high-resolution panchromatic image $\boldsymbol{Y}$. In another way, X can be considered as $\boldsymbol{Z}$ multiplying a down-sampling matrix $\boldsymbol{H}$, and panchromatic $\boldsymbol{Y}$ can also be up-sampled in spectral-domain by matrix $\boldsymbol{P}$. Thus, the super-resolution can be modeled as:

$$\min_{Z} \|X - ZH\|_F^2 + \|Y - PZ\|_F^2 + \lambda\phi(Z)$$

where $\|.\|_F$ denotes the Frobenius norm, and $\phi(Z)$ refers to an appropriate regularize derived from the intrinsic structure of $\boldsymbol{Z}$.

2.2. Spectral Evaluation

For the evaluation of spectrum quality, the consistency between the reconstructed spectrum and the original spectrum is taken as the first consideration. The main reason is that the spectral information should not be changed due to reconstruction. Therefore, the extremely distorted spectrum of single-pixel is first searched to understand the distortion of the reconstructed HSI. Subsequently, the distribution histogram of the pixel-level average spectral value in reconstructed HSI is displayed to investigate the distortion of the reconstructed spectrum. Then, the spectral Spearman correlation and spectral Euclidean distance between the low-spatial-resolution cube and the high-spatial-resolution cube are calculated to further quantitatively analyze the similarity between the reconstructed spectrum and the original spectrum. Because the scale factor is 20, each pixel (1×139) in the low spatial resolution HSI can correspond to a sub-cube (20×20×139) in the high spatial resolution HSI. When calculating the Euclidean distance and spearman correlation between the original spectrum and the reconstructed spectrum, the spectrum $\boldsymbol{s}$ of each pixel in low-spatial-resolution HSI is compared with the average spectrum $\bar{\boldsymbol{s}}$ of its corresponding sub-cube.

In addition, the endmembers of the original low-spatial-resolution cube and reconstructed high-spatial-resolution cube are also extracted and match with the abundance maps. This is also to analyze the consistency between the reconstructed HSI and the original HSI from the perspective of spectral components. The spectral endmembers directly depend on the materials of image content which is same before and after reconstruction. Ideally, spectral endmembers account for most of the image's spectral variability and serve as a reference to determine the spectral makeup of mixed pixels. Since the signature of each material can not be provided in this case, the Automatic Target Generation Process (ATGP) endmembers induction algorithm[15] is utilized to select a set of appropriate initial endmembers. And the abundance maps are also created to show the distribution of each endmember. This endmember analysis is vital to understand the spectrum consistency between original and reconstructed HSI. The similar endmembers and abundance map indicate the reconstructed HSI keeps the spectral features from the original low-spatial-resolution HSI. This endmember extraction is completed by PySptools.

2.3. Non-reference Image Quality Metrics (Spatial Domain)

For a comprehensive image quality evaluation, the spatial domain quality is another important part. However, there is no ground truth HSI in this case to complete the referenced image quality examination. Therefore, three non-reference statistics-features-based metrics are utilized to evaluate the spatial domain quality of reconstructed HSIs: 1). Blind/Referenceless Image Spatial Quality Evaluator (BRISQUE)[16], 2). Naturalness Image Quality Evaluator (NIQE)[17], and 3). Perception-based Image Quality Evaluator (PIQE)[18]. Herein, the PIQE range [0, 20] is excellent quality, [21, 35] is good quality, and [36, 50] is fair quality. For BRISQUE and NIQE, the lower the score, the better the image quality. Moreover, the non-reference scores are evaluated one layer by one layer since HSIs have multiple layers. And all the scores are calculated by MATLAB functions. The non-reference image quality scores of two HSIs ($\boldsymbol{I_1}$ and $\boldsymbol{I_2}$) are listed in Tab. 1. From the table, Cubert and Bayesian HSIs have better quality than other reconstructed HSIs according to scores. Based on PIQE scores, all reconstructed HSIs have at least good quality or better. This guarantees the HSIs used in spectral quality evaluation have the success spatial reconstruction.

Table 1. Non-reference Image Quality

		Cubert	*RCS*	*LMVM*	*Bayesian*	*Manifold*
$\boldsymbol{I_1}$	**BRIS.**	40.35	44.23	44.03	42.49	45.85
	NIQE	7.41	8.14	6.79	6.99	9.49
	PIQE	14.71	19.99	16.57	14.83	22.89
$\boldsymbol{I_2}$	**BRIS.**	38.84	33.56	33.97	32.65	46.55
	NIQE	8.06	5.51	4.98	4.72	10.06
	PIQE	23.04	25.31	22.62	21.84	28.42

3.EVALUATION RESULTS AND ANALYSIS

This research used two HSIs ($\boldsymbol{I_1}$ and $\boldsymbol{I_2}$) from the HSI dataset in [1] for image quality examination. But only $\boldsymbol{I_1}$'s reconstructions are shown in Fig. 1 considering the length of the paper. Here, (a) subfigure is produced by simplest bicubic interpolation, and it can be seemed as a baseline.

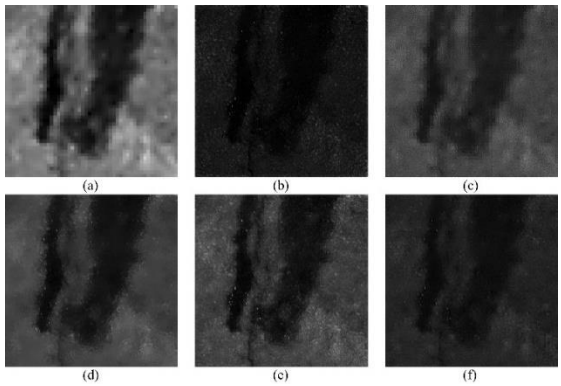

Figure 1 I_1 reconstruction results at 520nm. (a) Bicubic. (b) Cubert. (c) RCS. (d) LMVM. (e) Bayesian. (f)Manifold

3.1. Spectrum similarity

In the beginning, each reconstructed HSI is searched for the most abnormal pixels (with extremely high-value spectrum). Fig. 2 plots abnormal spectrums in the Cubert method reconstructed HSI and the corresponding original spectrums in low-spatial-resolution HSI. Especially, I_1 abnormal spectrum is already more than five times of original one.

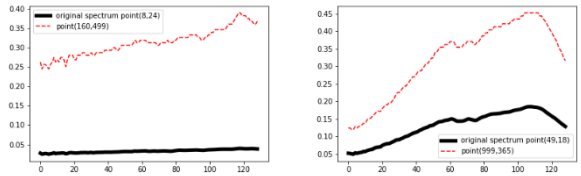

(a) (b)

Figure 2 Abnormal spectrum in Cubert HSI: (a) I_1 (b) I_2

Next, the average spectrum distribution histogram is plotted for a more comprehensive understanding (Fig. 3). Thereinto, subfigure (a) is the average spectrum distribution of low-spatial-resolution HSI. From the observation, the Cubert method (b) produced HSI has the most distorted distribution. And manifold-based reconstruction (f) has the most similar distribution to the original HSI. Although there is a shifting in the range of average spectrum in the other three reconstructed HSIs (c-e), the distributions still maintain the feature (a sunken part). Moreover, (b-e) distributions include a number of larger average spectrum values. In detail: the Cubert HSI has more than 800 pixels with over 9000 average spectrum. There are only 29 pixels' average spectrum are over 8000 in Bayesian fused HSI.

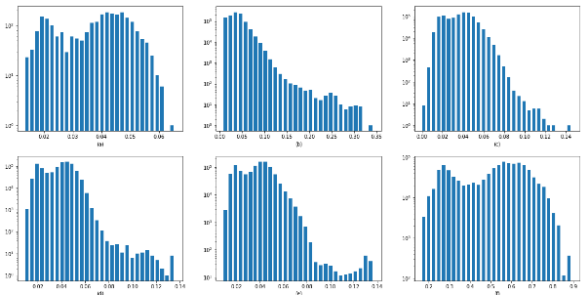

Figure 3 Average spectral value distributions of I1: (a) Origin; (b) Cubert; (c) RCS; (d) LMVM; (e) Bayesian; (f)Manifold

Finally, we calculate both Euclidean distance and Spearman correlation from the spectrum in original low spatial-resolution HSI to the patch-average spectrum in high spatial-resolution. Tab.2 lists the spectrum Euclidean distance and Spearman correlation. Except for Manifold reconstructed HSI, the other four reconstructed HSIs have very short distances and high correlation with the spectrum in original HSI. But the RCS reconstructed HSI has burred spatial quality (observe from Fig. 1). The possible cause is that the RCS reconstructed HSI simply by the weighed spectrum value; this leads the spatial details can not be rephrased in good quality. Moreover, the Bayesian fused HSI's spatial quality is closed to Cubert HSI (show in Fig. 1), but the Bayesian HSI has a shorter distance and higher correlation than Cubert HSI.

Table 2. Spectral Similarity

		Cubert	*RCS*	*LMVM*	*Bayesian*	*Manifold*
I_1	***Dist***	0.011	8.2e-7	0.021	0.0037	0.414
	Corr	0.984	0.999	0.973	0.9957	0.532
I_2	***Dist***	0.007	2.5e-7	0.015	0.005	0.515
	Corr	0.973	0.999	0.967	0.982	0.409

3.2. Endmembers and Abundance Maps

To understand the spectral quality of reconstructed HSIs from another perspective, the endmembers are extracted for spectral components analysis. The endmembers can represent the fundamental components of HSIs; therefore, similar endmembers indicate the reconstructed HSI maintains similar spectral properties as the original HSI. And the similar spectral components can justify that the spectral information does not change or loss after reconstruction. In Fig. 4, the endmember spectrums of each HSI are showed.

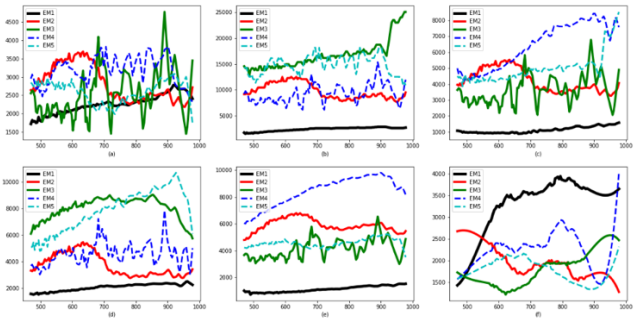

Figure 4 Endmembers of I_1: (a) Original. (b) Cubert. (c) RCS. (d) LMVM. (e) Bayesian. (f)Manifold

Generally, RCS and LMVM reconstructed HSIs have similar endmembers with low-spatial-resolution HSI because these two reconstructions are from weighed spectrum values in low-spatial-resolution HSI. This computation does not change spectral value a lot; thus, the endmembers are most similar. But the simple reconstruction also leads to a low spatial quality. Moreover, the Cubert method reconstructed HSI imports a few new type endmembers, such as the EM3. These new endmembers may be the source of the distortion in average spectrum distribution (Fig. 3 (b)). Furthermore, Bayesian fused HSI has consistent endmembers with low-spatial-resolution HSI. And these endmembers are smoother and more separated than original HSI's. The separability benefits the following operations, for example, classification or detection.

However, Manifold-based reconstructed endmembers are very different from original HSI. One possible reason is that the Manifold-based reconstruction is completed band by band, which breaks the spectral connections.

At the same time, the abundance maps of relative endmembers are demonstrated in Fig. 5. Although Cubert HSIs have very high quality in the spatial domain, the abundance of endmember distribution is most different from original HSI because of new endmember imported. And Bayesian fused HSIs keep very high similarity with original HSI and have fair spatial quality.

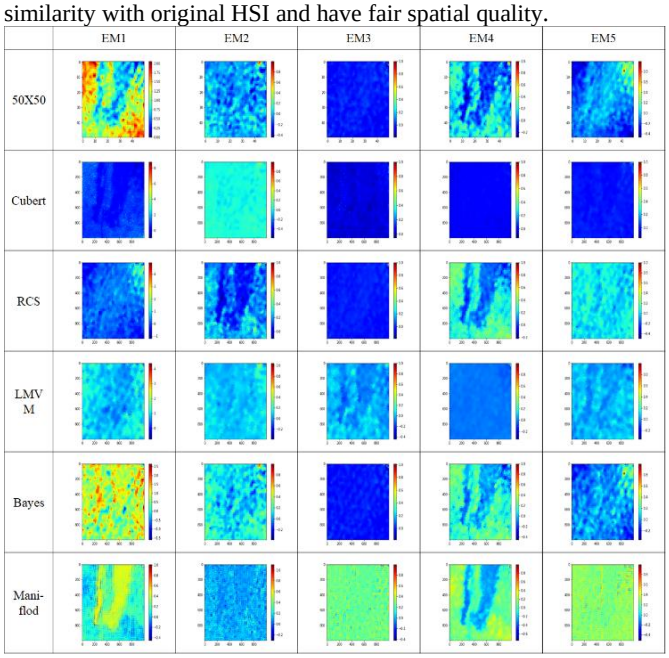

Figure 5 Abundance maps of I_1

3.3. SVM Experiment

A simple SVM classification is completed only based on spectral information to explore the relationship between high-spatial-resolution reconstruction and further procedures. The classification confusion matrixes of I_1 and I_2 are listed in Tab. 3. HSI I_1 has 4 classes of pixels: crack, water, oil, and background. And HSI I_2 also has 4 classes of pixels: crack, artificial color, green vegetation and background. Here, the crack means the line-damage on concrete or asphalt surface.

From the results, the oil and water are hard to distinguish only based on spectral information. And the crack pixels are either difficult to extract purely rely on the spectrum. It is worth mentioning that Bayesian HSI, which has more separated endmembers. With Bayesian reconstruction, background pixels recognition rate is slightly improved, and the fewer pixels are misclassified from water- and oil-classes into crack-class. Besides, sample I_2 illustrated a situation that the simple sharpening HSIs (RCS and LMVM) and original HSI trained SVM has good performance to distinguish oil, artificial color, and green vegetation pixels because these materials have unique spectrums. But the most background pixels are misclassified into the crack class. On the other side, the high spatial quality HSIs (Cubert and Bayesian) have very poor classification performance. This may provide clues that spatial quality improvement causes losing spectral features.

3.4. Discussions

This paper aims to explore more spectral quality in reconstructed high-spatial-resolution HSI than spatial quality because the valuable spectral information may lose or be adjusted after reconstruction. After the special evaluation of spectral quality in multiple HSIs produced by the Cubert method and four other methods, there are some points are worth discussing:

1) Trade-off between spatial and spectral quality

The spatial quality evaluation is generally based on the clear contour of the object purely in human-visual judgment. However, some spectral information may lose results in the pursuit of high spatial quality. For example, the more-clear Cubert HSI has different endmembers from the original HSI and leads to misclassification in I_2 SVM experiment. Therefore, an assumption can be made that the high spatial quality may not the final goal of high-spatial-resolution HSI reconstruction. Finding a balance in high spatial quality and authentic spectral properties might be more important than purely reaching clear images humans-visually-admitted because the more precise spectral information is most invisible.

2) Relationship between high-spatial-resolution reconstruction and subsequent processing

The high-spatial-resolution reconstruction is always the preprocessing of many computer vision tasks. It is commonly believed that high spatial quality can lead to high performance. However, the spectrum-based SVM experiment showed some uncommon phenomena where the clearer HSIs (Cubert and Bayesian) trained SVMs have worse performance in classification. Because the clearer HSIs may lose or adjust some spectral features when approaching a high spatial quality, the clearer HSIs trained SVMs lead to more misclassified samples. This also proves that the high-spatial-resolution reconstruction affects the subsequent operations in specific conditions.

4. CONCLUSIONS

This work focuses on evaluating the spectral quality of high-spatial-resolution HSIs reconstructed from low-spatial-resolution HSI captured by commercial snapshot hyperspctral camera – Cubert S185. Due to the lack of ground truth, it is difficult to evaluate the spectral quality in reconstructed HSI. This article proposed a *non-reference evaluation* scheme to evaluate the spectral quality of the reconstructed high-spatial-resolution HSI. The scheme includes the assessment of spectrum similarity computation and spctral component analysis. In addition, the primary SVM is trained with the reconstructed HSI to explore the relationship between high-spatial-resolution reconstruction and subsequent processing. The results show that the trade-off between spatial sharpening and spectral information maintenance is crucial to the correctness of spectral features.. Since high-resolution reconstruction may affect the spectral characteristics, some reconstructed HSIs with better spatial quality cause the worse classification performance. Although the spatial domain resolution improving is essential, the spectral domain reliability also influences the following processing, especially the spectrum-relative analysis. Thus, this paper can provide a reference for other Cubert camera users and researchers.

Table 3 SVM results

Note: C = Crack; W = Water; O = Oil; A = Artificial Color; G = Green Vegetation; B = Background

I_1	*Cubert*				*RCS*				*Bayesian*				*Manifold*				***Tot.***
	C	***W***	***O***	***B***	***C***	***W***	***O***	***B***	***C***	***W***	***O***	***B***	***C***	***W***	***O***	***B***	
C	1206	0	0	594	774	0	162	864	864	0	198	738	522	0	180	1098	1800
W	1170	0	450	180	252	0	1476	72	430	2	1242	126	810	18	900	72	1800
O	666	0	1026	108	162	18	1530	90	252	0	1476	72	648	0	1008	144	1800
B	162	0	18	1620	108	0	54	1638	72	0	36	1692	180	0	18	1602	1800
Tot.	3204	0	1494	2502	1296	18	3222	2664	1618	2	2952	2628	2160	18	2106	2916	7200

I_2	*Cubert*				*RCS*				*Bayesian*				*Manifold*				***Tot.***
	C	***A***	***G***	***B***	***C***	***A***	***G***	***B***	***C***	***A***	***G***	***B***	***C***	***A***	***G***	***B***	
C	1458	342	0	0	1566	108	0	0	1458	342	0	0	1404	360	0	0	1800
A	54	1746	0	0	90	1710	0	0	54	1746	0	0	90	1710	0	0	1800
G	0	0	1800	0	0	0	1800	0	0	0	1800	0	0	18	1782	0	1800
B	1656	90	54	0	1638	54	54	0	1656	90	54	0	1620	108	54	0	1800
Tot.	3726	3420	1854	0	3510	1872	1854	0	3726	3420	1854	0	3222	3798	1836	0	7200

5. REFERENCES

[1] S. Aryal, Z. Chen, and S. Tang, "Mobile Hyperspectral Imaging for Material Surface Damage Detection," *Journal of Computing in Civil Engineering*, vol. 35, no. 1, 2021.

[2] H. Aasen, A. Burkart, A. Bolten, and G. Bareth, "Generating 3D hyperspectral information with lightweight UAV snapshot cameras for vegetation monitoring: From camera calibration to quality assurance," *ISPRS Journal of Photogrammetry and Remote Sensing*, vol. 108, pp. 245-259, 2015/10/01/ 2015.

[3] S. Jakob, R. Zimmermann, and R. Gloaguen, "Processing of drone-borne hyperspectral data for geological applications," in *2016 8th Workshop on Hyperspectral Image and Signal Processing: Evolution in Remote Sensing (WHISPERS)*, 2016, pp. 1-5: IEEE.

[4] M. René, L. Sven, and G. Rainer, "Snapshot-Hyperspektroskopie," *Photonik*, pp. 36-38, 2014.

[5] N. Hagen and M. Kudenov, "Review of snapshot spectral imaging technologies," *Optical Engineering*, vol. 52 no. 9, p. 090901, 2013.

[6] M. West, J. Grossmann, and C. Galvan, "Commercial Snapshot Spectral Imaging: The Art of the Possible," ed, 2019.

[7] Q. Wei, J. Bioucas-Dias, N. Dobigeon, and J. Tourneret, "Hyperspectral and Multispectral Image Fusion Based on a Sparse Representation," *IEEE Transactions on Geoscience and Remote Sensing*, vol. 53, no. 7, pp. 3658-3668, 2015.

[8] C. Wang, Y. Liu, X. Bai, W. Tang, P. Lei, and J. Zhou, "Deep Residual Convolutional Neural Network for Hyperspectral Image Super-Resolution," 2017, pp. 370-380.

[9] A. R. Gillespie, A. B. Kahle, and R. E. J. R. S. o. E. Walker, "Color enhancement of highly correlated images. II. Channel ratio and "chromaticity" transformation techniques," vol. 22, no. 3, pp. 343-365, 1987.

[10] S. de Béthune, F. Muller, and J.-P. J. F. o. E. D. Donnay, Sophia, Antipolis, France,, "Fusion of multispectral and panchromatic images by local mean and variance matching filtering techniques," 1998.

[11] D. Fasbender, J. Radoux, and P. Bogaert, "Bayesian Data Fusion for Adaptable Image Pansharpening," *IEEE Transactions on Geoscience and Remote Sensing*, vol. 46, no. 6, pp. 1847-1857, 2008.

[12] L. Zhang, W. Wei, C. Bai, Y. Gao, and Y. Zhang, "Exploiting Clustering Manifold Structure for Hyperspectral Imagery Super-Resolution," *IEEE Transactions on Image Processing*, vol. 27, no. 12, pp. 5969-5982, 2018.

[13] C. Cortes and V. Vapnik, "Support-vector networks," *Machine Learning*, vol. 20, no. 3, pp. 273-297, 1995/09/01 1995.

[14] M. Grizonnet, J. Michel, V. Poughon, J. Inglada, M. Savinaud, and R. Cresson, "Orfeo ToolBox: open source processing of remote sensing images," *Open Geospatial Data, Software and Standards*, vol. 2, no. 1, p. 15, 2017/06/29 2017.

[15] A. Plaza and C. Chang, "Impact of Initialization on Design of Endmember Extraction Algorithms," *IEEE Transactions on Geoscience and Remote Sensing*, vol. 44, no. 11, pp. 3397-3407, 2006.

[16] A. Mittal, A. K. Moorthy, and A. C. Bovik, "No-Reference Image Quality Assessment in the Spatial Domain," *IEEE Transactions on Image Processing*, vol. 21, no. 12, pp. 4695-4708, 2012.

[17] A. Mittal, R. Soundararajan, and A. Bovik, "Making a "Completely Blind" Image Quality Analyzer," *Signal Processing Letters, IEEE*, vol. 20, pp. 209-212, 03/01 2013.

[18] N. Venkatanath, D. Praneeth, B. Maruthi Chandrasekhar, S. S. Channappayya, and S. S. Medasani, "Blind image quality evaluation using perception based features," in *2015 Twenty First National Conference on Communications (NCC)*, 2015, pp. 1-6.